Dissipation regimes for short wind waves

Guillemette Caulliez

▶ To cite this version:

HAL Id: insu-03621063
https://insu.hal.science/insu-03621063

Submitted on 27 Mar 2022

Dissipation regimes for short wind waves

Guillemette Caulliez[1]

[1]   The dissipation processes affecting short wind waves of centimeter and decimeter scales are investigated experimentally in laboratory. The processes include damping due to molecular viscosity, generation of capillary waves, microbreaking, and breaking. The observations were made in a large wind wave tank for a wide range of fetches and winds, using a laser sheet and a high-resolution video camera. The work aims at constructing a comprehensive picture of dissipative processes in the short wind wave field, to find for which scales particular dissipative mechanism may become important. Four distinct regimes have been identified. For capillary-gravity wave fields, i.e., for dominant waves with scales below 4 cm, viscous damping is found to be the main dissipation mechanism. The gravity-capillary wave fields with dominant wavelength less than 10 cm usually exhibit a train of capillary ripples at the crest wavefront, but no wave breaking. For such waves, the main dissipation process is molecular viscosity occurring through nonlinear energy cascade toward high-frequency motions. Microscale breaking takes place for waves longer than 10 cm and manifests itself in a very localized surface disruption on the forward face of the crest. Such events generate turbulent motions in water and thus enhance wave dissipation. Plunging breaking, characterized by formation of a crest bulge, a microjet hitting the water surface and a splash-up, occurs for short gravity waves of wavelength exceeding 20 cm. Macroscale spilling breaking is also observed for longer waves at high winds. In both cases, the direct momentum transfer from breaking waves to the water flow contributes significantly to wave damping.

1.   Introduction

[2]   A proper knowledge of dissipation processes affecting short wind waves of centimeter or decimeter scales is essential for adequate description of wave field evolution. However, these processes are not well understood yet and an overall picture of their conditions of occurrence is still lacking. In particular, the role of molecular viscosity, generation of capillary ripples, and microbreaking or breaking has not been clearly identified and quantified up to now. These dissipative processes contribute each in its own way to momentum transfer from waves to subsurface mean and turbulent water flows and thus can significantly affect the structure of the uppermost water boundary layer [*Terray et al.*, 1996; *Gemmrich and Farmer*, 2004; *Siddiqui and Loewen*, 2007; *Kudryavtsev et al.*, 2008]. Due to their crucial importance for refining parameterization of small-scale momentum and gas exchanges across the sea surface and hence for improving wave

[1]Mediterranean Institute of Oceanography, Aix-Marseille Université, Université du Sud Toulon-Var, CNRS/INSU, IRD, UM 110, Marseille, France.

Corresponding author: G. Caulliez, Mediterranean Institute of Oceanography, 163, avenue de Luminy, case 901, 13288, Marseille, Cedex 09, France. (guillemette.caulliez@univ-amu.fr)

modeling, studies of wave dissipation processes have raised an ever-increasing interest over the last decades.

[3]   Wave breaking is a commonly observed phenomenon at the sea surface for a wide range of wave scales and it has attracted most attention. A large number of experimental and theoretical works were aimed to better describe and model these fascinating events, the acquired understanding being summarized in reviews and books by *Banner and Peregrine* [1993], *Melville* [1996], *Duncan* [2001] and *Babanin* [2011]. In particular, the geometric properties of steady or wave-focused breaking waves and the related phenomena at the wave crest such as the formation of a plunging jet and the generation of turbulent patches and bubbles in water have been thoroughly investigated both experimentally by studying mechanically generated waves of meter scale and by means of numerical simulations [see for instance *Bonmarin*, 1989; *Rapp and Melville*, 1990; *Longuet-Higgins and Dommermuth*, 1997; *Xue et al.*, 2001]. Furthermore, significant progress has been made recently in determining wave parameters controlling the wave breaking onset and strength [*Song and Banner*, 2002; *Banner and Pierson*, 2007, *Drazen et al.*, 2008]. However, the common limitation of these studies is that they are confined to phenomena occurring in idealized two-dimensional wave groups. In independent investigations concerning smaller scales, the conspicuous generation of parasitic capillaries at the wavefront of short waves, typically less than 10 cm in wavelength, has been described extensively using similar experimental
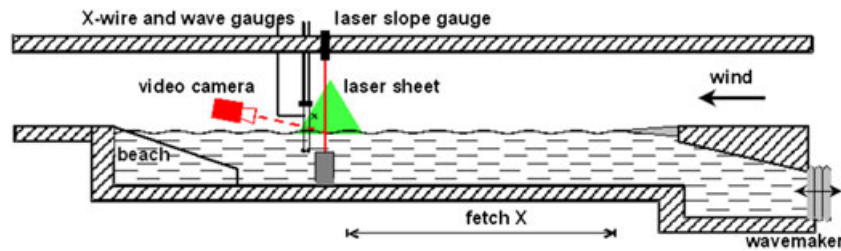
Figure 1. Schematic view of the experimental arrangement and the instrumentation set up in the large Luminy wind wave tank for wave visualizations.

or numerical approaches [*Cox*, 1958, *Ermakov et al.*, 1986; *Jiang et al.*, 1999; *Longuet-Higgins*, 1963, 1995; *Ruvinsky et al.*, 1991; *Fedorov and Melville*, 1998; *Hung and Tsai*, 2009]. Wave breaking phenomena in the range of decimeter wave scales, often called microbreakings, appear to be more difficult to model conceptually and to examine experimentally. Therefore, up to now there are only few works devoted to their investigation. For waves of wavelength shorter than 50 cm, numerical simulations have shown that capillary forces due to water surface tension prevent overturning of wave crests [*Tulin*, 1996; *Longuet-Higgins*, 1997]. Microbreaking is then marked at the surface by formation of a bulge on the forward face of the wave crest and a train of capillary ripples riding ahead, as observed experimentally by *Ebuchi et al.* [1987], *Duncan et al.* [1999], and *Diorio et al.* [2009]. After the pioneering works by *Banner and Phillips* [1974] and *Okuda* [1982], investigations of the water flow exploiting novel imaging techniques have clearly indicated that these surface disturbances are indeed accompanied by the development of a thin surface turbulent sublayer below the wave crest following a downward intrusion of water at the bulge toe [*Jessup et al.*, 1997; *Siddiqui et al.*, 2001; *Peirson and Banner*, 2003; *Zappa et al.*, 2004].

[4] Wind wave fields observed at sea or in large laboratory facilities are characterized by a broadband spectrum and a wide angular distribution. As a consequence, the basic features of naturally occurring wind wave breakers of various scales may differ greatly compared to those obtained from model wave experiments with mechanically generated waves or simulations based on quite simplistic wave models. Thus, in the range of short scales, the wave field conditions in which particular dissipation processes might occur have not been clearly determined yet. Among the still open issues we distinguish the following basic questions: (i) Should we consider parasitic capillaries upon gravity-capillary waves as microbreakers or do these waves keep a wave-like nature as described numerically by *Fedorov and Melville* [1998] and *Hung and Tsai* [2009]?; (ii) What is the wind wave wavelength above which typical macroscale breaking with jet formation and air entrainment may occur?; (iii) What are the distinctive features of wave motion which might enable us to detect microscale breaking events at the water surface?. The present work aims at addressing these questions and constructing a comprehensive picture of wave dissipation regimes.

[5] This study reports the first results of an experimental investigation of wind wave surface motions of centimeter and decimeter scales carried out in the large Marseille-Luminy wind wave tank for a wide range of wind speeds and fetches. Using visualizations of longitudinal wave profiles, the surface signatures of the various wave dissipation phenomena,

including wave microbreaking and breaking, are first described qualitatively for capillary-gravity to gravity-scale wind waves. The ranges of scales where each dissipative process can take place and may become dominant have been found. A few specific features of wave kinematics and dynamics associated with these regimes and breaking events have been identified.

2. Experimental Procedure

[6] Wind wave field observations were carried out in the large Marseille-Luminy wind-wave facility comprising a 40 m long, 2.6 m wide, and 0.9 m deep water tank and a recirculating air flow channel of 1.5 m height at the test section (Figure 1) [*Coantic and Favre*, 1975]. Steady winds varying between 1 and 14 m/s are generated by an axial fan located in the recirculation flume. The air flow channel which includes divergent and convergent sections, turbulence grids, and a test section of slightly increasing height, is specially designed to obtain a low-turbulence homogeneous flow at the entrance of the water tank and a constant-flux air boundary layer over the water surface. In addition, to avoid generation of large-scale air flow disturbances just over the surface boundary layer at the entrance of the water tank, a weakly inclined flexible device was fixed at the edge of the bottom floor of the air channel. This arrangement thus insures a smooth junction between the solid air channel floor and the water surface for all wind speed conditions. At the end of the water tank, a permeable beach damps the wave reflection. The instruments for wind and wave measurements were set up at a fixed position located at the 28 m fetch test section of the channel which is equipped with glass windows. Then, to adjust the measuring fetch, the upwind water surface was covered by a thin floating plastic sheet of variable length.

[7] Visualizations of wind wave surface profiles along the wind direction were performed by means of a vertical plane light sheet and a high-resolution monochrome digital video camera. The light sheet was generated by means of a 4 W Ar$^+$ laser and an optical head fixed immediately at the end of the laser beam fiber transmitter and set up in the air flow at a distance of 40 cm from the tank sidewall. The water was seeded by fluorescein dye for sharpening the light contrast of the air-water interface. A MegaPlus ES 4.0 video camera was mounted outside the facility test section, looking down through the glass side window with a tilt angle of 8°. The 2000×640 pixel images corresponding to a field of view of approximately 23 cm in the horizontal direction with a pixel resolution of 0.116 mm were captured at a frame rate of 15 Hz. The exposure time was chosen in a range of values between 3 and 6 ms, depending on wave phase speed. At 26 m fetch, a set of images were also captured at a frame rate
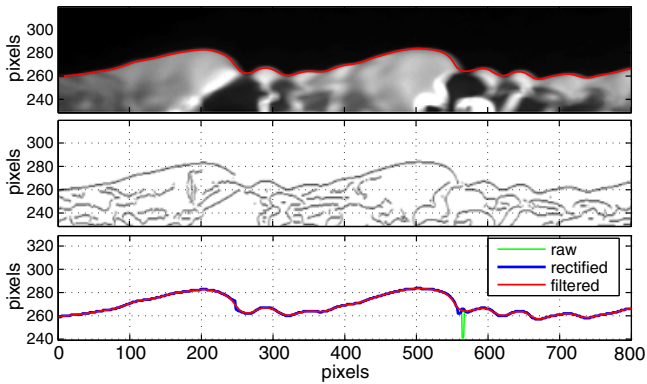
Figure 2. (a) Enlarged view of a typical image captured at 6 m fetch and 5.0 m/s wind speed in which is reported the wave profile as obtained ultimately after smoothing by a Gaussian filter ($\sigma = 5$). (b) Contours extracted from this image by using a Canny edge detection method. (c) Wave profile as obtained immediately after a direct detection of the water surface contour (green line), after the correction of the small raw profile defects (blue bold line) and after smoothing by a Gaussian filter of standard deviation 5 (red line).

of 400 Hz, using a fast-speed video camera (model Phantom V5). The image size was 1024×512 pixels and the exposure time was 2.49 ms.

[8] To extract the wave profiles from the images, an original software based on the *Canny* [1986] edge detection method was developed. This algorithm is built on the detection of the local luminance gradient maxima using two successive gradient magnitude thresholds after applying a smoothing of the original images with a Gaussian filter of 0.85 pixel in standard deviation. Then, the surface contour lines are primarily identified as the first maxima found when moved vertically from the air to the water flow. The raw profiles thus obtained are analyzed to remove 1 pixel noise spikes higher than 5 pixels by linear interpolation. The broader spikes due to the presence of droplets in air were also eliminated by tracking the adequate luminance gradient maxima in the immediate vicinity of the surface contour lines detected on both sides of such spikes. Finally, the spikes oriented toward the water flow caused by the absence of luminance gradient extrema at the air-water interface were removed by using a linear interpolation. These "black" zones are observed in surface areas of large enough positive curvature to induce strongly divergent laser light refraction. At the very end of the image processing routine, a Gaussian filtering is applied to the wave profiles in order to smooth the tiny remaining noise defects. The standard deviation of the filter is chosen in accordance with the type of data analysis to be performed. Here, it was fixed to be 5 pixels. The last procedure enables us to take the first and second derivatives of the surface contour lines to estimate the corresponding longitudinal wave slope and curvature signals. Note that at this stage of development, this image processing software is unable to detect surface wave contours of slope higher than 90° in absolute value. We can also mention that the blurring effect generated in the images by the wave displacement during the exposure time is typically of order of 15 pixels in such image capture conditions and is essentially akin to a window filtering of the surface contour lines. As the

dye particles at the water surface move along the interfacial streamlines when waves propagate downstream, nonlinearities or bias introduced in the surface contour detection method by this motion look negligible. Only a little noise may affect the detection process associated with the decrease of the luminance gradient magnitude on the water surface. Consistently, the final resolution of the "average" wave profile detection method is of order of 1.8 mm at best. To illustrate the main steps of the image processing procedure, a snapshot of the raw profile and its final smoothed version is shown in Figure 2, in comparison with the original wave image and the water surface contour as obtained directly by using the Canny edge detection method.

[9] In addition to wave visualizations, measurements of wave elevation and wave slopes in two directions were performed by means of two capacitance wave probes and a single-point laser slope optical system located at the immediate vicinity of the laser sheet. The air flow velocity field and the surface wind stress were monitored by a Pitot tube and X-wire probes. The first series of experiments was carried out at four fetches between 2 and 26 m, and for 6–7 wind speeds ranging from 3 to 10 m/s. For each couple of wind and fetch conditions, six to eight series of 300 images were recorded by means of the high-resolution video camera in parallel with the wind velocity, wave elevation, and surface slope signals. Complementary wave visualizations by using the fast-speed video camera were made at 26 m fetch for 9 wind speeds between 2.5 and 12 m/s. The characteristic properties of air flow and wave fields derived from single-point probe measurements for the various wind and fetch conditions investigated here are reported in Table 1.

3. Wave Profile Analysis

[10] Figure 3 displays a typical side view of the wave field as captured by the high-resolution video camera (Figure 3a) combined with two graphs with records of five successive wave contours and the respective computed longwise wave slope samples (Figures 3b and 3c). The displayed profiles are numbered, and the corresponding number is reported in the left bottom corner of the image in Figure 3a. Such wave profiles are characteristic of wave fields with dominant waves of a few centimeters wavelength observed at small fetches for moderate wind speeds (a wider view from above of the various wave fields described here can be found in *Caulliez and Collard* [1999, Figure 2; this reference will be denoted *CC99* hereinafter]). For the 5.5 m/s wind speed and 2 m fetch conditions reported in Figure 3, the wave height is of order of 1 mm and the average dominant wavelength rates 3.7 cm when estimated over the whole set of images by means of an autocorrelation method applied to extracted wave profiles (see Table 1). The successive wave contours show that these capillary-gravity wave motions exhibiting typical round crests and sharper troughs are rather random both in scale and height. Furthermore, each wave profile is only poorly correlated with the previous one observed 66 ms before. This corroborates the fact that the wave field is widely distributed both in scale and in wave propagation direction as shown in *CC99*. Although tiny, the wave motions exhibit quite high slopes on both sides of the deeper troughs, the slopes reaching the values of ± 0.5 (i.e., $\pm 30°$). Visual analysis of the whole set of images recorded

for these wave field conditions, as well as the related wave contours, indicates no manifestation of surface disruption resulting from the trough collapse with the formation of one trapped bubble. For capillary-gravity waves, this phenomenon takes place when the water surface on both sides of the trough becomes vertical and then touches, as described by *Chen and Saffman* [1980]. Thus, these observations would indicate that such a singular wave breakdown does not occur at this stage of wave development, at least when wave fields are not too strongly forced by wind as observed in the present work.

[11] Figure 4 presents in a similarly organized plot five wave profiles observed at 5 m/s wind speed and 6 m fetch. This wave field is representative of the next stage of wind wave development, the water surface being covered by gravity-capillary waves (denoted GCW in the following) with conspicuous parasitic capillaries at the front of the crests and forming rhombic patterns [*CC99*]. The analysis of wave contours and the related longitudinal wave slopes reveals a distinctly different pattern: almost all waves exhibit an asymmetric crest with a characteristic round bulge at the wavefront and a train of well-shaped ripples developing ahead. The amplitude and the wavelength of such ripples decrease with the distance to the bulge toe. Furthermore, these GCW of about 6 cm in wavelength and 0.5 cm in height propagate at a robustly constant phase speed, of approximately 40 cm/s. This feature is illustrated in Figure 4c by
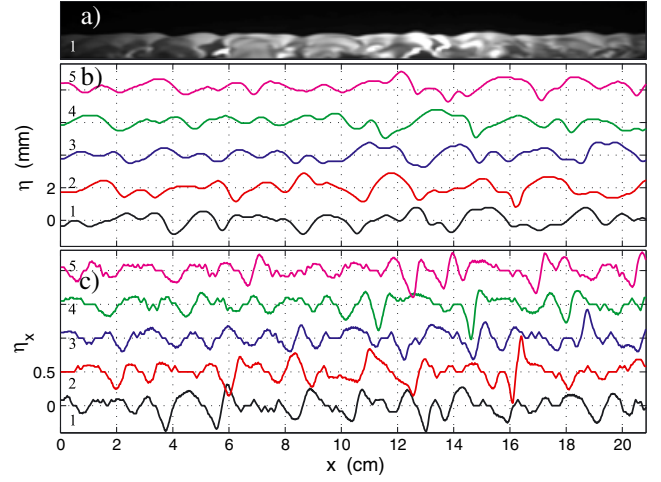

Figure 3. Longitudinal wave profiles observed in the large wind wave tank at 2.0 m fetch and 5.5 m/s wind speed: (a) typical image viewed from the side by the camera, the wind blowing from left to right; (b) wave contours extracted from five successive realizations captured at 66 ms time interval (time increases from bottom to top and the zero shift of each contour is given by the y axis scale); and (c) longitudinal wave slope of the respective numbered contours.

Table 1. Mean Wind and Wave Properties Observed During Wave Profile Visualization Experiments[a]

Fetch (m)	U_{ref} (m/s)	u^* (m/s)	f_p (Hz)	λ_p (cm)	A_d (mm)	ak_d	$Rmss_d$	C_{max}	λ_{im} (cm)	Regime Type
2	5	0.16	11.0	2.8	0.06	0.02	0.25	0.09	3.2	I
	5.5	0.17	10.8	3.0	0.20	0.05	0.28	0.17	3.7	I
	6	0.19	9.3	3.4	0.26	0.06	0.27	0.28	4.0	I
	7	0.23	8.3	4.1	0.40	0.08	0.27	0.24	4.8	II
	8	0.30	7.3	4.9	0.73	0.11	0.30	0.26	6.0	II
	10	0.35	5.5	8.7	1.95	0.15	0.31	0.15	10.0	II-III
6	4	0.13	9.2	3.7	0.15	0.03	0.21	0.30	4.3	I-II
	5	0.17	6.9	5.4	0.76	0.10	0.28	0.30	6.4	II
	6	0.22	5.7	7.5	1.4	0.13	0.31	0.30	8.7	II
	7	0.27	4.8	11.3	2.3	0.14	0.31	0.23	11.6	III
	8	0.32	4.0	15	3.5	0.16	0.40	0.08	14.3	III
	9	0.38	3.6	18	4.3	0.16	0.37	0.06	17.7	III
13	3	0.08	6.9	5.4	0.4	0.05	0.24	0.34	5.1	II
	4	0.14	5.1	8.9	1.4	0.12	0.31	0.20	8.4	II
	5	0.19	4.0	14	2.9	0.15	0.29	0.19	12.6	III
	6	0.24	3.3	19	4.0	0.16	0.26	0.06	16.8	III
	7	0.29	3.0	23	5.6	0.16	0.36	0.02	-	IV
	8	0.35	2.8	26	6.1	0.17	0.42	-	-	IV
	9	0.41	2.6	32	7.4	0.17	0.41	-	-	IV
26	2.5	0.07	5.3	7.7	0.8	0.08	0.22	-	-	II
	3	0.10	4.0	13	1.7	0.10	0.23	-	-	III
	4	0.15	3.0	21	3.2	0.12	0.20	-	-	III
	5	0.20	2.5	30	5.3	0.13	0.20	-	-	IV
	6	0.25	2.3	36	7.1	0.14	0.21	-	-	IV
	7	0.31	2.1	42	8.5	0.14	0.31	-	-	IV
	8	0.35	2.0	46	10.0	0.15	0.30	-	-	IV
	10	0.49	1.8	58	14.3	0.16	0.37	-	-	IV
	12	0.63	1.6	75	18.4	0.18	0.33	-	-	IV

[a]Average properties of air flow and wind wave fields. All the quantities are derived from single-point probe measurements except the two last ones. U_{ref} is the reference wind speed measured at the center of the air tunnel; u^* is the air friction velocity at the water surface; f_p is the dominant spectral peak frequency; λ_p is the dominant wavelength derived from the spectral peak frequency and the mean longitudinal phase velocity estimated by a cross-correlation method using two wave probe signals; A_d and ak_d are the average dominant wave height and dominant wave steepness estimated by computing the respective wave elevation and total wave slope spectral peak energy between 0.5 and $1.5f_p$; $Rmss_d$ is the ratio of crosswise to alongwise mean square slope of dominant waves; λ_{im} is the dominant wavelength derived from the abscissa of the first maximum of the average normalized auto-correlation function of longitudinal wave profiles; C_{max} is the level of this function at the first maximum, i.e., a quantity inversely proportional to the dominant spectral peak width: it might be seen as an indicator of the sine wave model relevance for describing such wave profiles of limited length and then an indicator of the accuracy of the wavelength estimation method.
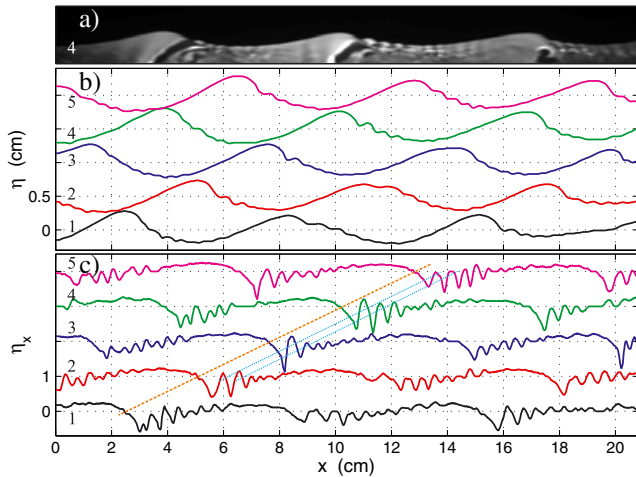
Figure 4. Longitudinal wave profiles at 6 m fetch and 5.0 m/s wind speed. The graph is organized as Figure 3.

plotting a straight line connecting the downward zero crossings of the successive wave slope samples, i.e., the x location of the maxima of wave crest elevation. Note that this phase speed estimate corresponds to the longwise component only. The wave slope records also show that the trains of capillary waves generally include at least four ripples of wavelength shorter than approximately 6 mm. The highest negative slope of order one is observed at the bulge front of the dominant wave crest or, sometimes, at the first ripple wavefront. For most capillary wavetrains, the two first ripples move at the same speed as the dominant wave crest. This can be visualized in the same way as described above: the straight line connecting the ripple crest abscissas is parallel to those connecting the dominant wave crests. Another illustration of this quasi-steady wave behavior observed at 26 m fetch and 2.5 m/s wind speed for waves of lower steepness is given in Animation 1 in the supporting information. In this short sequence, a group of well-formed gravity-capillary waves of roughly 6 cm in wavelength propagates downstream with practically no deformation while a long train of tiny persistent capillaries (up to 11 wavelets) corrugates the forward dominant wavefront and trough. This wave behavior strongly suggests that the formation of capillaries is due to the development of nonlinear resonant interaction between the dominant GCW and the capillary waves propagated ahead as first suggested by *Cox* [1958] and more recently described in detail by *Fedorov and Melvill*e [1998] and *Hung and Tsai* [2009]. This justifies entirely the attribute "parasitic" in referring to such capillary ripples even when generated by gravity-capillary *wind* waves. It also would mean that surface motions observed in these conditions may be described within the framework of nonlinear wave theories. In such conditions, most of the energy pumped from wind into the wave field is dissipated by capillaries [*Tsai and Hung*, 2010]. Thus, at moderate wind speeds, the air-water interface disruption is prevented by effective nonlinear dissipation.

[12] Wave profiles typical of longer gravity-capillary wind wave fields are shown in Figure 5. These waves of 12 cm average wavelength were observed at 6 m fetch and 7 m/s

wind speed. Visual observations of the water surface and a more detailed wave profile analysis show that such wave fields are very similar to those of shorter scale described previously as both exhibit three-dimensional GCW with asymmetric round crest and trains of capillaries propagating forward. However, these ripples are noticeably shorter and of smaller height, not exceeding 5 and 0.8 mm for the most prominent ones. The wavetrains mostly present a smaller number of well-shaped parasitic waves, usually three. The actual number is likely higher, but the smaller ripples can be missed because of the low resolution of the wave imaging and processing techniques (see for instance the capillaries rippling the first crest of wave profile 4 in Figure 5). Indeed, one can observe directly from the images by using lighting effects long wavetrains of minute ripples propagating over almost the whole dominant trough making clearly distinguishable by the presence of light stripes visible in the image water side up to the surface but not directly discernible on wave profiles (in Figure 5a, see this phenomenon on the very left side of image 5). As for the shorter waves, the highest negative longitudinal wave slope, of order one, is observed on the forward face of the dominant wave crest just before the bulge toe. However, occasionally steeper dominant crest wavefront can be found, being usually followed downstream by random short-scale surface disturbances rather than a regular capillary wavetrain. The shape of the second wave crest of profiles 3 and 4 in Figure 5 (marked by arrows) illustrates quite well this wave feature. The surface roughness ruffling the forward face of the crest and more particularly distinguishable in
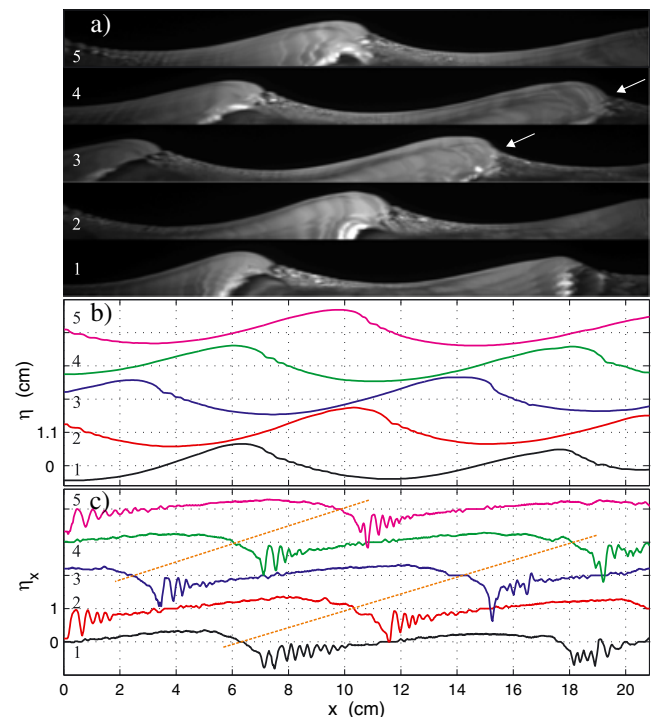

Figure 5. Longitudinal wave profiles observed at 6 m fetch and 7.0 m/s wind speed. The graph is organized as Figure 3 except that the five images corresponding to the five wave contours given in Figure 5b are displayed in Figure 5a. The arrows indicate the microbreaking wave crest.
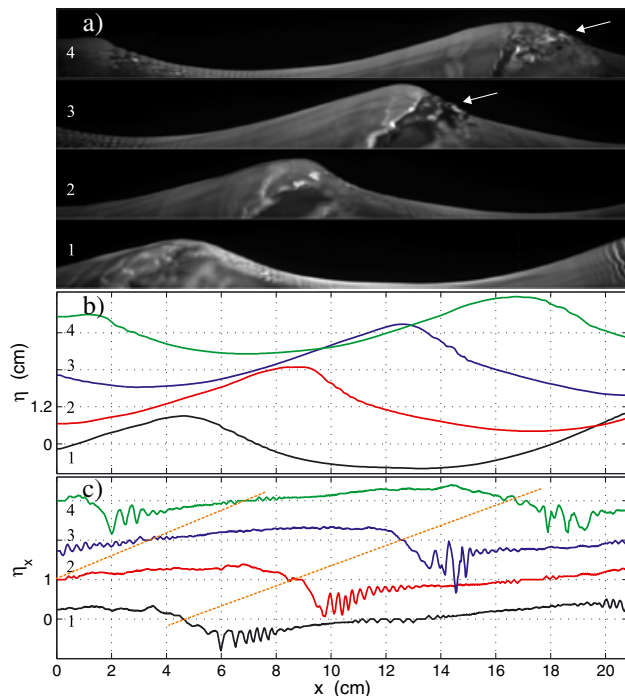
Figure 6. Longitudinal wave profiles observed at 13 m fetch and 6.0 m/s wind speed. The graph is organized as Figure 3 except that four images and the related four wave contours and longitudinal wave slope signals are given in Figures 6a–6c. The arrows indicate the microbreaking wave crest.

the related slope sample strongly suggests the occurrence of a localized breakdown of the GCW crest. Such events that generate turbulent motions in the air and water flows and a rough zone at the interface can be identified as microbreakings. For these events, the water surface no longer remains a streamline but the turbulent motions and the associated pressure fluctuations are not large enough for generating bubbles. As a matter of fact, no bubbles were detected for these wave fields, neither by observing visually the water surface nor from a survey of all wave images. Nevertheless, the wave crest breakdown which occurs at the bulge toe and generates subsurface turbulence may be revealed by the development of a wavetrain of tiny ripples propagating in all directions around this localized surface disturbance. This can be seen in a striking way in Animation 2 in which the steep wave crest with very short capillaries ahead visualized on the image right suddenly breaks 14 s later the start of the sequence. Meanwhile, minute undulations propagating against the wind are generated at the bulge toe and released behind the crest before vanishing. The occurrence of such an against-the-wind wavetrain is a remarkable visual signature of microbreaking event (see also Figure 5a). Finally, we can point out that the microbreaking wave crest generally moves at a faster phase speed than the wave crest and the wave trough immediately upstream, as clearly shown in Figure 5 (there, the wave crest moves at 59 cm/s rather than 54.5 cm/s).

[13] Figure 6 displays four successive wave images observed at 13 m fetch and 6 m/s wind speed, as well as the related wave profiles and longitudinal surface slopes. The short gravity wave field visualized in these conditions is characterized by an average wavelength of about 17 cm

and a significant height of order 2 cm. As shown only partly in this figure due to the limited size of the field of view, the wave field appears to be composed of two main types of wave motions. First, waves of shape very similar to those of the GCW described previously, i.e., waves with a round bulge and a train of capillaries propagating on the forward face of the crest, frequently occur at the water surface. They generally coincide with the shortest waves of the wave field, sometimes of very small amplitude, as for instance the first wave crest of profile 4 displayed in Figure 6. In this case, steady short ripples of less than 5 mm in wavelength propagate at the front of the wave crest but are short lived, evolving during hardly one dominant wave period. Otherwise, waves of more pyramidal shape but slightly asymmetric are seen occasionally at the water surface, generally inside the most pronounced wave groups. Therefore, they are the highest and longest waves of the wave field. From time to time, it occurs that their crest wavefront steepens and breaks down, thus creating turbulent motions in water and large irregular disturbances on the forward face of the wave. Such surface manifestations of water turbulence can be seen in the two last wave images displayed in Figures 6a.3 and 6a.4. Just prior to breakdown, a train of very tiny and short capillaries may be generated on the crest wavefront but a round crest bulge is not ever discernible, presumably due to three-dimensional effects (Figures 6a.1 and 6a.2). The wave crest breakdown itself may generate short-lived irregular surface protuberances and more long-lived trains of larger-scale ripples. No more than one bubble however has been detected per sequence of 300 images. One can also notice that the breaking wave crest moves at a constant phase speed without any acceleration during its steepening phase, but the velocity is a little higher than those of the wave trough just upstream. In Animation 3, a video sequence captured at 26 m fetch and 4 m/s wind speed also shows the evolution of a typical short gravity wave during its steepening phase with the formation of a crest bulge and the fast development of capillary ripples. Then, such a change in wave shape is immediately followed by the crest breakdown, as clearly seen at 4 s time.

[14] The short gravity wave fields associated with the further stages of wave development by wind as observed in the water tank are of longer wavelength than the width of the camera field of view, so only portions of single wave profiles can be analyzed from the available wave images. Accordingly, the average wavelength is determined only approximately from wave elevation time series. In addition, the variability and the complexity of wave motions observed in a set of images increase, making the comprehensive analysis of wave fields more difficult to perform. So, in the rest of the paper, only two striking wave breaking events which occur for waves of roughly 25 cm and 75 cm in wavelength will be described qualitatively.

[15] The first sequence of images presented in Figure 7 was observed at 13 m fetch and 8 m/s wind speed and shows a sort of "plunging" breaking, i.e., a quite unexpected phenomenon because it concerns a very short wave for which capillary forces are expected to be still effective for preventing a jet formation at the crest [*Tulin*, 1996; *Longuet-Higgins*, 1997]. As seen in Figure 7a.1, the initial breaking stage is characterized by the occurrence of an almost overturning wave crest exhibiting a very pronounced bulge on its upper
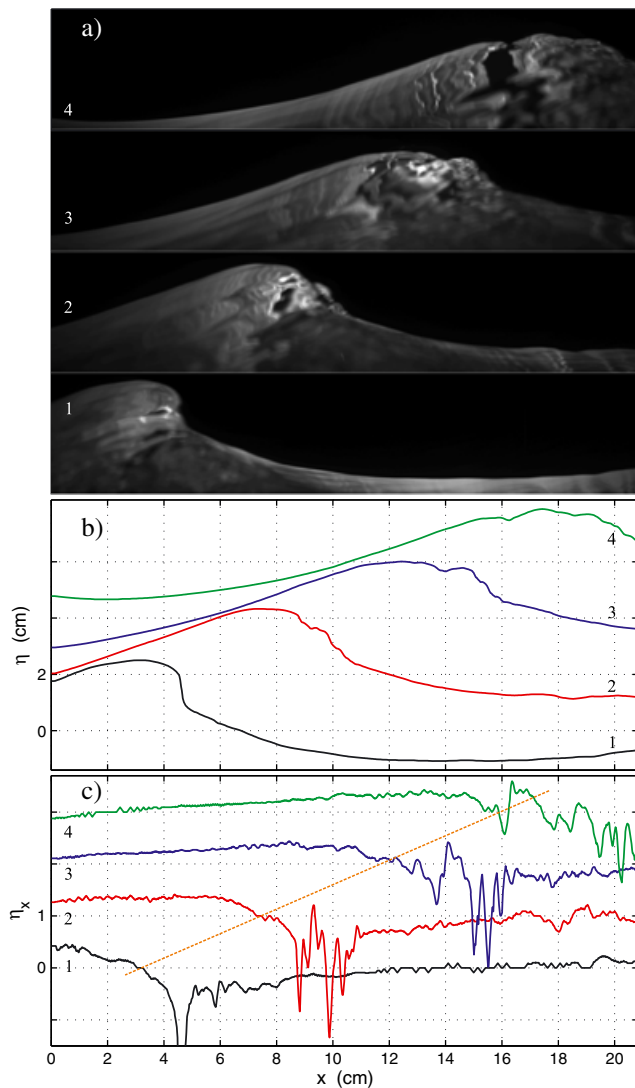
Figure 7. Longitudinal wave profiles observed at 13 m fetch and 8.0 m/s wind speed. The graph is organized as Figure 6. This particular plunging breaking wave has a wavelength of approximately 25 cm.

forward face. Let us recall that the edge detection method used here does not enable to detect the reversed slope contour seen in the image, so the detailed shape of the bulge is not well described by the respective wave elevation and wave slope signals. We can also point out here that the wave crest is preceded by a remarkably flat trough. In the second image (Figure 7a.2), the crest protrusion evolves forward until it gives rise to a small water jet projecting out from the mid part of the wave front face and impacting the water surface slightly ahead of the crest. The dark zone observed between the small jet and the wavefront suggests the formation of a little cavity of air. This plunging microjet generates a small water splash-up impacting in turn the water surface further downstream (Figures 7a.2 and 7a.3). The wave crest breakdown develops until the fluid ejections degenerate into a patch of turbulence spreading inside the upper water flow and marked at the surface by small round bumps and wavy corrugations (Figure 7a.4). Note that the succession of phenomena visualized in Figure 7 lasts 0.2 s, i.e., roughly half

a wave period. Compared to what happens for shorter waves, it seems that at the later stage of the wave breakdown (profiles 3 and 4), the crest moves at a slightly higher velocity than those observed at the initial stage of breaking (profiles 1 and 2), as indicated by the straight line plotted in Figure 7c. On the contrary, the maximum (negative) mean slope of the crest wavefront is reached at the onset of breaking, then it decreases from -0.75 for the first profile to -0.35 for the third one, this quantity being estimated between the point where the wave crest is the highest and the following wave profile downward zero-crossing. At last, just mention that despite the occurrence of such plunging wave breaking at these wind and fetch conditions, only few bubbles are seen at the water surface, visually or by watching the wave images. Animation 4 presents a video sequence observed at 26 m fetch and 7 m/s wind speed; it shows the same type of plunging breaking event for a short gravity wave of similar wavelength (of order of 30 cm in this case). As the wave crest is more likely to be oriented obliquely rather than perpendicularly to the laser sheet plane, the first microjet ejected from the crest wavefront foot as seen at 5 s time from the start of the video is less distinguishable here. Otherwise, this breaking event is characterized by a succession of noticeable splashes-up and ejections, leading to air bubble entrainment. Such a phenomenon manifests in the images by intense laser light flashes. The latter occur when single bubbles emerge from water and break the surface.

[16] A sequence of wave images recorded by the fast-speed video camera at 26 m fetch and 12 m/s and revealing the development of a spilling wave breaking in its most active phase is displayed in Animation 5. In addition, Figure 8 presents a few snapshots of this video sequence to emphasize the most significant wave breaking features. The average wavelength of the wind-generated gravity wave field is approximately 75 cm. The pictures clearly show that macroscale spilling breaking can be seen as a succession of small plunging water jet and splash-up events, associated with substantial air entrainment in water and spray generation in air. Thus, in the first snapshot of Figure 8, one can easily distinguish a well-formed plunging microjet at the crest wavefront. The microjet is hitting the water surface and thus generates a small splash-up ahead it. By visualizing the previous images, it seems that the microjet is not the first one created during this breaking event because the latter has already started upstream but in an area not specifically aligned with the laser sheet, the wave crest being oriented obliquely to the wind direction. Further downstream, the rather flat wave trough exhibits just small undulations, very likely due to capillary-gravity waves generated directly by wind, and thus does not appear to be affected by the breakdown of the following crest. The second image shows the same microjet and the associated splash-up at a later stage of development, both ejections being sustained by new fluid when the wave crest moves downstream. One can notice the formation of a mixture of air and water at the point of impact of the jet and inside the splash-up, this bubbly fluid of white color being even recycled in the secondary splash-up rising ahead the first one. The four following images show the emergence of a single microjet and its development during a rather long period. Note that owing to the variability of the turbulent water flow just below the wave crest surface, the fluid ejection certainly varies in time. In fact, the
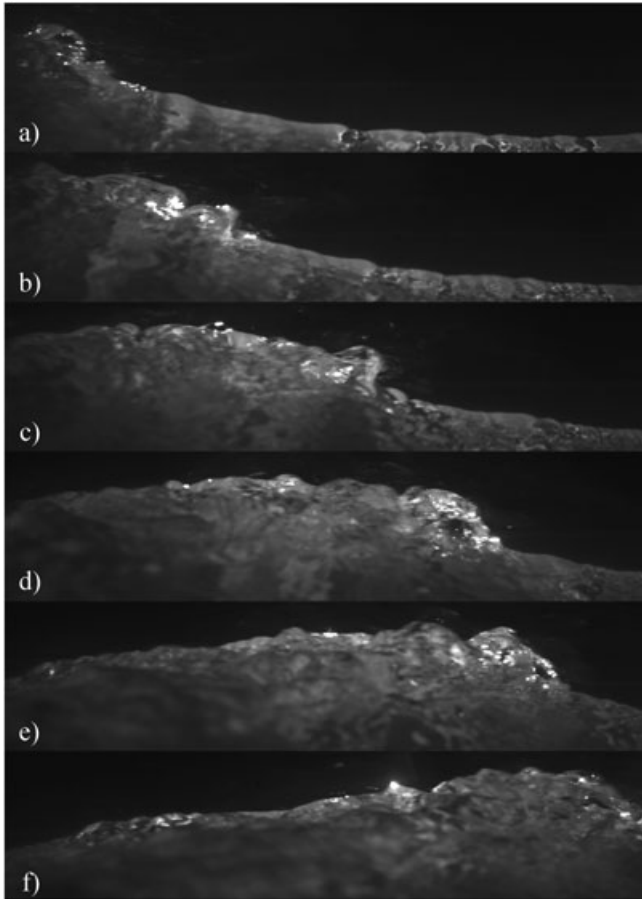
Figure 8. Snapshots of a spilling breaking wave recorded by the fast-speed video camera at 26 m fetch and 12.0 m/s wind speed and captured at the respective times: (a) 0 ms, (b) 3.75 ms, (c) 7.75 ms, (d) 10.75 ms, (e) 13.75 ms, and (f) 17.75 ms. This particular breaking wave has a wavelength of approximately 75 cm.

instantaneous velocity field results from complex interaction processes between surface motions and the air flow above as well as the wave motions and the water turbulence itself. An idea of the stress intensity exerted by such a gale-force wind at the surface is revealed when noticed in all Figure 8 images, the presence of many spray droplets and even spumes torn out the fluid ejections as white "smoke" blowing into the air. Finally, respectively in the third and the last images, a thin water film and a round bubble piercing the surface are seen, indicating that the bubbles formed by dislocation of air cavities embedded in fluid ejections or air entrainment into water at the microjet impact points then burst at the water surface on the rear of the wave crest.

4. Discussion and Concluding Remarks

[17] The investigation of the wave profile images captured in the large wind-wave tank for a wide range of wind and fetch conditions gave us a better insight into dissipation mechanisms affecting short wind waves of centimeter to decimeter scales. First, recall that there are essentially two classes of wave dissipation process: wave dissipation due to viscosity and wave dissipation caused by breaking. The first process results from the work of viscous forces in water

leading to transformation of the wave potential and kinetic energy into heat. Wave breaking has to be associated with a water surface sublayer disruption which occurs when fluid particles initially at the surface escape it. During such events, the water surface does not remain a wave streamline any longer. Therefore, wave dissipation by breaking can be regarded as an energy transfer from waves to the flow in the interior, contributing primarily to the increase in both the mean and turbulent kinetic energy of the drift current, and also to the potential and kinetic energy of surface waves of various scales then generated by the surface breakdown. The qualitative description performed above reveals that there are different ways by which viscous and breaking phenomena manifest themselves. For small-scale wind wave fields, the main controlling parameter distinguishing the situations where these processes can play a role was found to be the wave scale.

[18] The detailed analysis of the whole set of images and movies first indicates that wave breaking affects only wind waves of wavelength larger than approximately 10 cm. For waves of shorter scale, wave dissipation by viscosity and nonlinear energy transfer to lower frequency waves appears to impede wave steepness growth efficiently enough for preventing waves from reaching a nonlinear shape with a singular breaking point, even when forced by moderate to strong wind. From a kinematical viewpoint, one can also argue that the orbital velocities induced by such wave motions at the crest, of the order of few centimeters per second in this wavelength range [*Hogan*, 1985; *Hung and Tsai*, 2009], are too small for matching the wave phase speed and correspondingly, for causing wave breaking. In this range of wave scales where viscous processes are dominant, we distinguish two qualitatively different regimes: (i) capillary-gravity waves of wavelength smaller than about 4 cm affected directly by viscous damping and (ii) short gravity-capillary waves for which the wave energy is dissipated through the generation of parasitic capillaries subjected to viscous dissipation. This process has been extensively investigated experimentally and numerically in the recent works by *Zhang* [2002] and *Tsai and Hung* [2010]. When considered quasi-monochromatic waves of a given initial steepness, we can infer from these studies that the enhanced dissipation rate due to the formation of parasitic ripples strongly depends on wave scale: the respective computed and observed damping parameters take the highest values for the shortest waves of length 3.9 cm and then decrease sharply beyond 7 cm. At 10 cm wavelength, the damping rate obtained from numerical simulations even remains comparable to the linear dissipation rate. For wind wave fields, a similar behavior could be expected but with a shift to a higher wavelength, since the wave dispersion relation and the related resonant wave-wave interaction condition for triggering ripple formation are likely to be affected by the wind-induced drift current. To investigate this effect and thus to test whether wave dissipation for gravity-capillary wind waves indeed occurs through the generation of parasitic capillaries, an analysis of the geometrical properties of capillary ripples was performed as function of the properties of the related carrier wave, as reported in Figure 9 for one series of 300 images. The procedure for evaluating these quantities is described in detail in Appendix A. Figure 9a displays the variation of the wavetrain-averaged
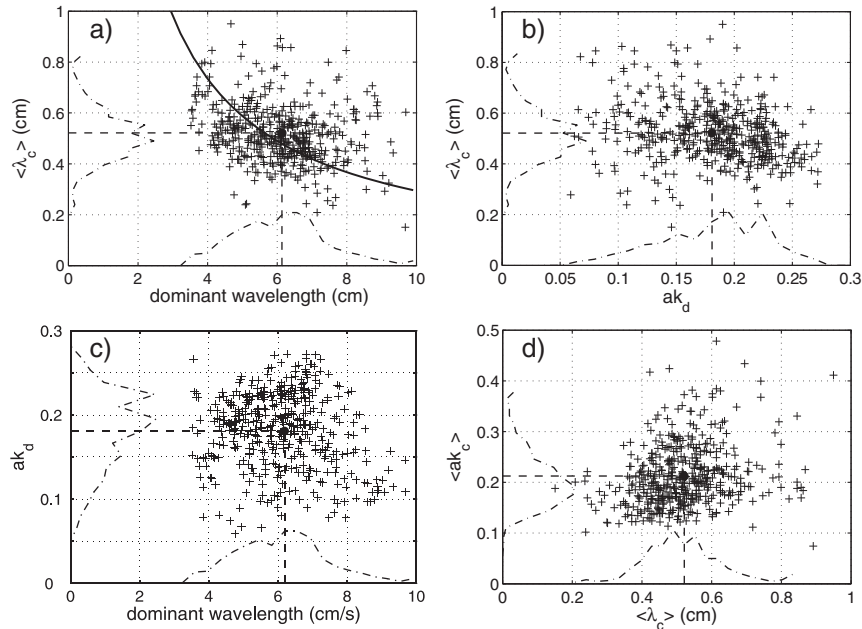
Figure 9. (a) Wavetrain-averaged wavelength of parasitic capillaries versus wavelength of the individual dominant carrier wave as observed for one series of 300 images captured at 5 m/s wind speed and 6 m fetch. The solid line corresponds to the resonant wave-wave interaction condition for free waves; (b) wavetrain-averaged wavelength of parasitic capillaries versus dominant carrier wave steepness; (c) dominant carrier wave steepness versus dominant wavelength; and (d) wavetrain-averaged steepness versus wavetrain-averaged wavelength of parasitic capillaries. The histograms of these various wave quantities are also reported in the respective figures (dotted dashed lines). The black dots and the dashed lines indicate the average quantity values estimated for this set of images.

parasitic ripple wavelength $\langle \lambda_c \rangle$ versus wavelength of the carrier gravity-capillary wave. The curve corresponding to the resonant conditions for free waves is plotted for comparison. This figure first reveals the great variability in space and time of individual wave characteristics, the ripple wavelength as well as the carrier wave length varying by more than 50% on both sides of their average values. Despite this large scatter, one can see that the wavelength of parasitic capillaries, of order of 5 mm here, tends to follow the resonant curve, decreasing when the dominant wavelength increases. No trend indicating a particular $\langle \lambda_c \rangle$ dependence on dominant steepness is found, the scatter in $\langle \lambda_c \rangle$ being only a bit smaller for dominant waves of higher steepness (Figure 9b). As systematically observed for all gravity-capillary wind wave fields investigated in this study, the average ripple wavelength does not fit exactly the resonant condition for free waves, being shifted to a slightly higher value. It is however difficult to determine whether this shift is due to a small change in length and time scales of interacting waves due to the surface drift current, or rather a change of the carrier wave characteristics within wave groups occurring after the ripple generation, or just a bias introduced by the length scale averaging. Figure 9d also shows that the average ripple steepness is weakly dependent on ripple wavelength, smaller steepness being observed for the shortest and then the most sporadic capillaries. These observations thus strongly suggest that the capillary ripples generated at the crest of gravity-capillary waves shorter than 10 cm result from such a resonant wave-wave interaction process. The ripples being rapidly damped by viscosity, this phenomenon contributes extensively to the carrier wave energy dissipation. Note that the percentage

of dominant waves exhibiting parasitic ripples in the wave field increases significantly when the average dominant wave steepness increases, i.e., when wind increases.

[19] For this set of experiments, it is also of interest to mention that parasitic capillaries have been noticed for carrier waves as long as 18 cm but in this case, it is difficult to distinguish whether their formation should be ascribed to a pure nonlinear wave-wave interaction process or the first manifestation of an incipient wave microbreaking event (for instance, see Animation 3). At the present stage of analysis, we can just point out that the scales of parasitic capillaries observed in these conditions depart significantly from the resonant conditions, their wavelength being quite systematically much longer.

[20] For gravity-capillary waves of wavelength exceeding 10 cm, we found in a conspicuous way that a very localized wave breakdown might occur at the wave crest when the wavefront becomes steep enough (Animation 2). To explain this qualitative change in behavior, one possibility would be that the capillaries generated by such longer waves get too tiny for providing wave dissipation for the whole wave field at a rate large enough for balancing wind energy input, even when accounting for the energy flux to longer scales due to nonlinear wave-wave interactions and responsible for frequency downshifting. Consequently, the average wave field steepness as well as the steepness of the individual waves propagating inside wave groups increases in such a way that breaking occurs. However, for wind waves of just one decimeter scale, we can expect that the energy transfer from waves to turbulent motions in water resulting from such microscale breaking events remains quite small. The
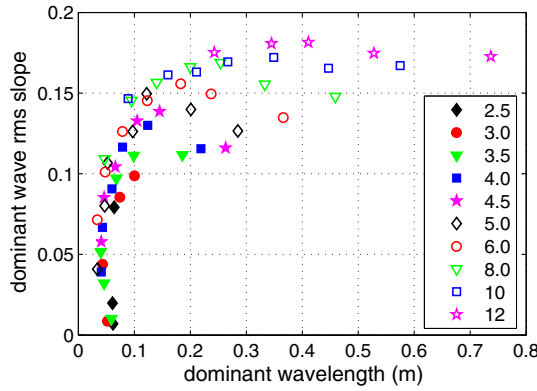
Figure 10. Variation of the RMS slope of dominant waves with dominant wavelength, as observed for various wind and fetch conditions in the large Marseille-Luminy wind wave tank. The legend gives the wind speed values in meters per second.

microbreaking events are first discernible by the formation of quite long capillaries induced by the pressure singularity arising at the surface sublayer disruption point when the water flow separation takes place. Therefore, most of the dissipated dominant wave energy is likely to be transferred to these waves of shorter scales. The breaking occurring for short gravity waves at a wavelength just below 20 cm is more distinctive, inasmuch as in such cases, surface manifestations of the turbulent motions generated in water can be clearly detected. We refer these wave crest breakdowns generating turbulent motions but no bubbles in water to microbreaking. For wave fields of average wavelength above 10 cm, the higher efficiency of microbreaking for dissipating wave energy compared to the parasitic capillaries generation, the former process leading to the generation of longer ripples and turbulent motions in water, is also shown by the sharp slowing down of the growth rate of the dominant wave root mean square slope (or even the decrease), as clearly noticeable in Figure 10 for all wind speeds. However, the variation of this parameter in its whole results from a complex interplay between wind input and wave dissipation phenomena. Thus, the detailed analysis of the dominant wave energy budget required for describing it precisely is postponed to a subsequent paper. At this stage of the discussion, we should just emphasize again that for a given wind wave field, different types of wave dissipation or breaking processes can coexist as wind waves evolve in well-shaped wave groups and three-dimensional patterns. These wave field features may explain not only the large scatter of the individual dominant wave steepness observed but also the high variability of the dominant wavelength, its typical range of variation being of order of ±50% around the average value.

[21] Macroscale breaking with generation of significant turbulence patches in water and bubbles starts to occur for gravity wind wave fields of wavelength just longer than 20 cm. Moreover, in contrast to the numerical simulations by *Tulin* [1996] and *Longuet-Higgins* [1997], these observations reveal that plunging wave breaking with formation of a crest bulge, a microjet and a splash-up can occur for very short gravity waves. A possible reason of this apparent discrepancy may come from the unavoidable contamination of the water surface by surfactants which modify slightly gravity wave breaking processes, as strikingly shown by *Liu and Duncan* [2003] for mechanically generated meter-scale waves. In particular, this might explain an odd feature exhibited by such short plunging breaking waves, namely the formation of a microjet at the mid or the foot of the wavefront rather than at the most prominent part of the bulge. Further investigation is needed to clarify the origin of this phenomenon. Here we can just outline that the water surface film was collected at the end of the water tank at the beginning of each day and no significant change in water surface tension was found during the observations, the measured value of this quantity with or without addition of fluorescein in water ranging around $73 \pm 1 \, \mathrm{dyn \, cm^{-1}}$. Finally, this study corroborates the fact that sporadic or more persistent spilling gravity wave breaking as commonly seen at the water surface for moderate to strong winds consists of a succession of water ejections taking place at the forward face of the wave crest and resulting from the formation of fluid microjets and splashes-up. The air trapped inside the embedded fluid ejection cavities or the air bubbles entrained at the microjet impact points then create a white mixture of air and water at the bumpy top of the wave crest. Our wave image analysis substantiates the idea that wind speed has no direct impact on the intrinsic nature of wave breaking, the breaking type advent being primarily controlled by the dominant wave scale. However, if we consider that breaking process is triggered when a local wave parameter dependent on wave steepness reaches a certain threshold as shown by *Song and Banner* [2002] and *Banner and Peirson* [2007], wind speed which controls the wave field average steepness and thus the range of variation of the individual wave steepness inside wave groups, then affects the frequency of occurrence and the strength of breaking events.

[22] In summary, this analysis of the submeter-scale wind wave profiles enables us to identify four regimes of wave dissipation primarily dependent on wave scale and
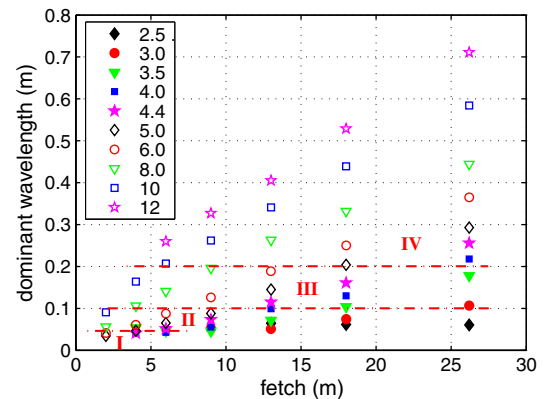

Figure 11. Dominant wavelength versus fetch diagram showing the conditions for which the different wave types and wave dissipation processes are observed in the water tank: (I) capillary-gravity waves dissipated by molecular viscosity; (II) gravity-capillary waves dissipated by generation of capillaries; (III) gravity-capillary waves dissipated by generation of capillaries and microscale breaking; and (IV) short gravity waves dissipated by macro- and microscale breaking. The legend gives the wind speed values in meters per second.
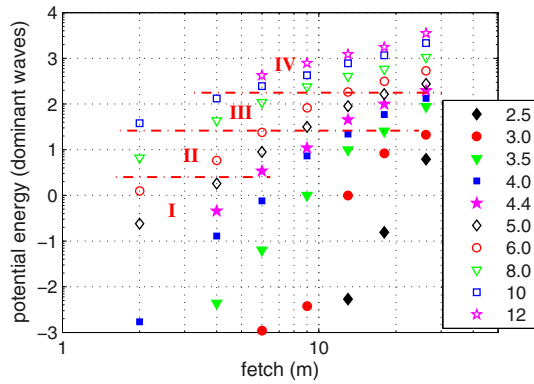
Figure 12. Evolution with fetch of the total potential energy ($\mathrm{J\,m^{-2}}$) of dominant waves as observed in the water tank for various wind speeds (the speed values in $\mathrm{m\,s^{-1}}$ are given in the legend box). The red lines delimit the four regimes of wave dissipation: (I) capillary-gravity waves dissipated by molecular viscosity; (II) gravity-capillary waves dissipated by generation of capillaries; (III) gravity-capillary waves dissipated by generation of capillaries and microscale breaking; and (IV) short gravity waves dissipated by macro- and microscale breaking.

associated with the successive occurrence of four distinct modes of wave dissipation, as represented schematically in Figure 11. The first regime concerns capillary-gravity waves of wavelength typically less than 4 cm for which wave dissipation results from a direct damping of fluid motions by molecular viscosity. The second regime of wave dissipation is observed for gravity-capillary wind wave fields of wavelength roughly shorter than 10 cm. In this range of wave scale, in addition to the direct viscous damping, which acts for all scales but with an efficiency sharply decreasing with scale, wave dissipation is essentially due to generation of parasitic ripples. This phenomenon can occur even for winds as low as 1.8 m/s, but then only occasionally. Parasitic capillaries result from a nonlinear resonant wave-wave interaction mechanism which develops as wave steepness increases. This process is responsible for efficient direct transfer of wave energy from gravity-capillary to capillary scale motions, the latter being rapidly damped by molecular viscosity. The third wave dissipation regime characterized by the occurrence of wave microbreaking concerns gravity-capillary wind wave fields of dominant wavelength exceeding 10 cm. The microbreaking leads to generation of turbulent motions in water and "new" ripples at the water surface; it contributes directly to wave damping and acts in parallel with the previous mechanisms. In this range of scale, the wave crest breakdown associated with such event is not energetic enough for generating bubbles. The physical processes leading irreversibly an individual wave to microbreaking and the wave parameters involved such as the existence of a critical wave steepness, have not been identified yet, primarily because of the great complexity of wave evolution intrinsic to the three-dimensional behavior of wind wave fields (due to both the development of 3-D wave patterns and the 3-D structure of wave groups). The fourth regime of wave dissipation is found for short gravity wind wave fields of wavelength exceeding 20 cm: for such waves, micro-plunging breaking or spilling

breaking become possible. The characteristic dramatic wave crest breakings are responsible for more intense generation of turbulent motions in water and bubble formation, thus increasing the wave energy dissipation. Finally, we mention that for wind wave fields as observed in a wind wave tank, each regime corresponds to a specific range of magnitude of the dominant wave potential energy, as shown in Figure 12. The respective thresholds for observing wave microbreaking or macroscale breaking events typical of the third and fourth mode of wave dissipation are found to be of order of 30 and 200 J cm^{-2}, while the total potential energy of capillary-gravity wind wave fields for which the first mode of wave dissipation takes place alone does not exceed 3 J cm^{-2}. This finding is directly linked to the self-similar nature of wind-generated wave fields as described by *Badulin et al.* [2007], the dominant wave frequency downshifting and the increase in the total wave field energy then being dependent. This result may open new perspective for parameterization of these short wind wave dissipative processes. A further step in this direction should consist in a better characterization of the distribution of wave properties around their average value for the various wave dissipation regimes. However, before attempting to extend these results to in situ wave field conditions, further work should be made, in particular to understand the role played by short wave modulations by long waves on such centimeter- to decimeter-scale wave dissipation phenomena.

Appendix A: Analysis of the Individual Wave Properties

[23] Wave contours extracted from the images enable us to determine a number of geometrical properties of parasitic capillaries in relation with those of the associated carrier gravity-capillary wave (GCW). To that end, a procedure using wave profiles and their first and second x derivatives was developed, as illustrated schematically in Figure A1A1. At first, the individual GCW observed in the images were identified by means of a classical method based on the detection of successive zero up-crossings of water surface displacements. Straightforwardly, the wavelength λ_d and the height h_d of each dominant wave were determined by rating respectively the distance between the corresponding zero up-crossings and the difference between the wave elevation maximum and minimum over this x interval. The related dominant wave steepness was evaluated using the following definition:

$$\gamma_d = \pi h_d / \lambda_d.$$

[24] Parasitic waves are characterized by large negative surface curvature at the crest and even higher positive curvature at the trough. Such ripple wavetrains generated at the front of GCW are clearly distinguishable by the occurrence of large oscillations of amplitude decreasing with the distance to the crest in the associated surface curvature samples estimated from the wave profile second x derivative. Using this feature, the capillary ripples were detected in such samples by searching for peaks of curvature higher of 1.5 cm^{-1} and located between the top of the carrier wave crest and the first wave elevation zero up-crossing just downstream. This threshold in wave curvature was chosen for selecting
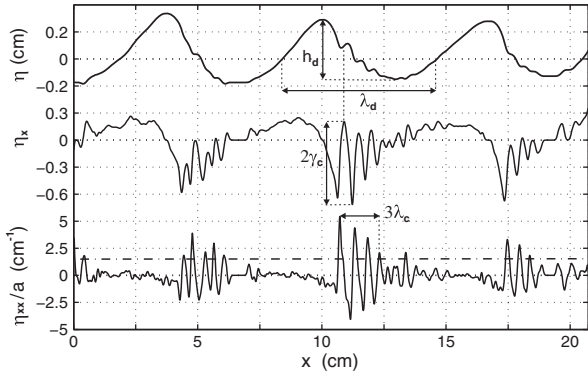
Figure A1. Typical longitudinal profiles of wave elevation η, longitudinal wave slope η_x, and wave curvature η_{xx}/a with $a = (1 + \eta_x^2)^{3/2}$. The characteristic wavelength λ_d and height h_d of an individual dominant wave as reported in Figure 9 are indicated in the plot as well as the characteristic scales of parasitic capillaries (the wavetrain-averaged ripple wavelength $\langle \lambda_c \rangle$, i.e., here $3 \langle \lambda_c \rangle = 3\lambda_c$, and the individual ripple steepness γ_c).

the most conspicuous capillaries, mostly located just ahead the gravity-capillary wave bulge. For each wavetrain, the average wavelength of the capillaries of curvature higher than $1.5 \, \text{cm}^{-1} \langle \lambda_c \rangle$ was estimated by computing the x distance between the first and the last curvature maxima (i.e., between the first and the last ripple troughs). The mean ripple steepness $\langle \boldsymbol{\gamma_c} \rangle$ was also estimated by averaging the individual ripple steepness, the latter being evaluated from the difference between the related maximum and minimum of the wave profile first derivative divided by 2. The geometrical quantities estimated for each ripple wavetrain and the corresponding carrier GCW were reported in Figure 9 for one series of images captured at 6 m fetch and 5 m/s wind speed.

[25] Physically, the generation of parasitic capillaries at the front of GCW can be interpreted as the development of a resonant nonlinear wave-wave interaction process between the basic wave component and its higher harmonics of order N [see for instance *McGoldrick*, 1972; *Chen and Saffman*, 1979; *Fedorov and Melville*, 1998]. The resonant condition associated with this phenomenon is satisfied at the first order when the linear phase velocity of capillaries matches those of the carrier wave. This relationship can be expressed as follows:

$$c_c = c_d \quad for \quad k_c = Nk_d,$$
$$\text{with} \quad c_c^2 = g/k_c + Tk_c \text{ and } c_d^2 = g/k_d + Tk_d,$$

where k_c and c_c are respectively the resonant capillary wave number and phase speed, k_d and c_d are respectively the resonant carrier wave number and phase speed, g is the gravity, and T is the surface tension normalized by the water density. By introducing in the linear dispersion relation, the wave number of the minimal wave phase speed k_m, namely $k_m^2 = g/T$, we obtain

$$c^2 = (gT)^{1/2}(k_m/k + k/k_m),$$

and the resonant condition can be satisfied when

$$k_d = N^{-1/2}k_m \text{ and } k_c = N^{1/2}k_m, \text{ i.e. , } k_d k_c = k_m^2.$$

The resonant curve $\lambda_d \lambda_c = \lambda_m^2$ was reported in Figure 9a.

References

Babanin, A. (2011), Breaking and Dissipation of Ocean Surface Waves, Cambridge Univ. Press, U.K.

Badulin, S. I., A. Babanin, V. E. Zakharov, and D. Resio (2007), Weakly turbulent laws of wind-wave growth, *J. Fluid Mech.*, *591*, 339–378.

Banner, M. L., and W. L. Peirson (2007), Wave breaking onset and strength for two-dimensional deep-water wave groups, *J. Fluid Mech.*, *585*, 93–115.

Banner, M. L., and D. H. Peregrine (1993), Wave breaking in deep water, *Annu. Rev. Fluid Mech.*, *25*, 373–397.

Banner, M. L., and O. M. Phillips (1974), On the incipient breaking of small-scale waves, *J. Fluid Mech.*, *65*, 647–656.

Bonmarin, B. (1989), Geometric properties of deep-water breaking waves, *J. Fluid Mech.*, *209*, 405–433.

Canny, J. (1986), A computational approach to edge detection, *IEEE Trans. Pattern. Anal. Mach. Intell.*, *8*(6), 679–698.

Caulliez, G., and F. Collard (1999), Three-dimensional evolution of the wind waves from gravity-capillary to gravity range, *Eur. J. Mech. B/ Fluids*, *18*(3), 389–402.

Chen, B., and P. G. Saffman (1979), Steady gravity-capillary waves on deep water. I: Weakly nonlinear waves, *Stud. Appl. Math.*, *60*, 183–210.

Chen, B., and P. G. Saffman (1980), Steady gravity-capillary waves on deep water. II: Numerical results for finite amplitude, *Stud. Appl. Math.*, *62*, 95–111.

Coantic, M., and A. Favre (1975), Activities in, and Preliminary Results of, Air-Sea Interactions Research at IMST, Advances in Geophysics, 18, Part A, pp. 391–405, Elsevier, Cambridge, Mass.

Cox, C. S. (1958), Measurements of slopes of high-frequency wind waves, *J. Marine Res.*, *16*(3), 199–225.

Diorio, J. R., X. Li, and J. H. Duncan (2009), An experimental investigation of incipient spilling breakers, *J. Fluid Mech.*, *633*, 271–283.

Drazen, D. A., W. K. Melville, and L. Lenain (2008), Inertial scaling of dissipation in unsteady breaking waves, *J. Fluid Mech.*, *611*, 307–332.

Duncan, J. H. (2001), Spilling breakers, *Annu. Rev. Fluid Mech.*, *33*, 519–547.

Duncan, J. H., H. Qiao, V. Philomin, and A. Wenz (1999), Gentle spilling breakers: Crest profile evolution, *J. Fluid Mech.*, *379*, 191–222.

Ebuchi, N., H. Kawamura, and Y. Toba (1987), Fine structure of laboratory wind-wave surfaces studied using optical methods, *Bound. Layer Meteor.*, *39*, 133–151.

Ermakov, S. A., K. D. Ruvinsky, S. G. Salashin, and G. I. Freidman (1986), Experimental investigations of the generation of capillary-gravity ripples by strongly nonlinear waves on the surface of a deep fluid, *Izv. Atmos. Oceanic Phys.*, *22*, 835–842.

Fedorov, A. V., and W. K. Melville (1998), Nonlinear gravity-capillary waves with forcing and dissipation, *J. Fluid Mech.*, *354*, 1–42.

Gemmrich, J. R., and D. M. Farmer (2004), Near-surface turbulence in the presence of breaking waves. *J. Phys. Oceanogr.*, *34*, 1067–1086.

Hogan, S. J. (1985), Particle trajectories in nonlinear gravity-capillary waves, *J. Fluid Mech.*, *151*, 105–119.

Hung, L.-P., and W.-T. Tsai (2009), The formation of parasitic capillary ripples on gravity-capillary waves and the underlying vortical structures, *J. Phys. Oceanogr.*, *39*, 263–289.

Jessup, A. T., C. J. Zappa, and H. Yeh (1997), Defining and quantifying microscale wave breaking with infrared imagery, *J. Geophys. Res.*, *102* (10), 23145–23153.

Jiang, L., H.-J. Lin, W. W. Schultz, and M. Perlin (1999), Unsteady ripple generation on steep gravity-capillary waves, *J. Fluid Mech.*, *386*, 281–304.

Kudryavtsev, V., V. Shrira, V. Dulov, and V. Malinovsky (2008), On the vertical structure of wind-driven sea currents, *J. Phys. Oceanogr.*, *38*(10), 2121–2144.

Liu, X., and J. H. Duncan (2003), The effects of surfactants on spilling breaking waves, *Nature*, *421*, 520–523.

Longuet-Higgins, M. S. (1963), The generation of capillary waves by steep gravity waves, *J. Fluid Mech.*, *16*, 238–259.

Longuet-Higgins, M. S. (1995), Parasitic capillary waves: A direct calculation, *J. Fluid Mech.*, *301*, 79–107.

Longuet-Higgins, M. S. (1997), Progress toward understanding how waves break, in Twenty-First Symposium on Naval Hydrodynamics, National Academy, Washington, DC, 7–28.

Longuet-Higgins, M. S., and D. G. Dommermuth (1997), Crest instabilities of gravity waves. Part 3. Nonlinear development and breaking, *J. Fluid Mech.*, *336*, 33–50.

McGoldrick, L. F. (1972), On the rippling of small waves: a harmonic nonlinear nearly resonant interaction, *J. Fluid Mech.*, *52*, 725–751.

Melville, W. K. (1996), The role of surface-wave breaking in air-sea interaction, *Annu. Rev. Fluid Mech.*, *28*, 279–321.

Okuda, K. (1982), Internal flow structure of short wind waves. Part I. On the internal vorticity structure, *J. Oceanogr. Soc. Japan*, *38*, 28–42.

Peirson, W. L., and M. L. Banner (2003), Aqueous surface layer flows induced by microscale breaking wind waves, *J. Fluid Mech.*, *475*, 1–38.

Rapp, R. J., and W. K. Melville (1990), Laboratory measurements of deep-water breaking waves, *Philos. Trans. R. Soc. Lond., Ser. A*, *331*, 735–800.

Ruvinsky, K. D., F. I. Feldstein, and G. I. Freidman (1991), Numerical simulations of the quasi-stationary stage of ripple excitation by steep gravity-capillary waves. *J. Fluid Mech.*, *230*, 339–353.

Siddiqui, M. H. K., M. R. Loewen C. Richardson, W. E. Asher, and A. T. Jessup (2001), Simultaneous particle image velocimetry and infrared imagery of microscale breaking waves. *Phys. Fluids*, *13*(7), 1891–1903.

Siddiqui, M. H. K., and M. R. Loewen (2007), Characteristics of the wind drift layer and microscale breaking waves. *J. Fluid Mech.*, *573*, 417–456.

Song, J., and M. L. Banner (2002), On determining the onset and strength of breaking for deep water waves. Part 1: Unforced irrotational wave groups, *J. Phys. Oceanogr.*, *32*, 1269–1283.

Terray, E. A., M. A. Donelan, Y. C. Agrawal, W. M. Drennan, K. K. Kahma, A. J. Williams, P. A. Hwang, and S. A. Kitaigorodskii (1996), Estimates of kinetic energy dissipation under breaking waves. *J. Phys. Oceanogr.*, *26*, 792–807.

Tsai, W.-T., and L.-P. Hung (2010), Enhanced energy dissipation by parasitic capillaries on short gravity-capillary waves, *J. Phys. Oceanogr.*, *40*, 2435–2450.

Tulin, M. P. (1996), Breaking of ocean waves and downshifting, in Waves and Nonlinear Processes in Hydrodynamics, (Eds. J. Grue, B. Gjevik & J. E. Weber), Kluwer Acad., Dordrecht, 177–190.

Xue, M., H. Xu, Y. Liu, and D. K. P. Yue (2001), Computations of fully nonlinear three-dimensional wave-wave and wave-body interactions. Part 1. Dynamics of steep three-dimensional waves, *J. Fluid Mech.*, *438*, 11–39.

Zappa, C. J., W. E. Asher, A. T. Jessup, J. Klinke, and S. R. Long (2004), Microbreaking and the enhancement of air-water transfer velocity, *J. Geophys. Res.*, *109*, C08S16, doi:10.1029/2003JC001897.

Zhang, X. (2002), Enhanced dissipation of short gravity and gravity-capillary waves due to parasitic capillaries, *Phys. Fluids*, *14*(11), L81–L84.